PCCP

PAPER

View Article Online
View Journal | View Issue

Cite this: *Phys. Chem. Chem. Phys.*, 2019, **21**, 3106

Air-stable formamidinium/methylammonium mixed lead iodide perovskite integral microcrystals with low trap density and high photo-responsivity†

Guangbao Wu,[a] Jiyu Zhou,[a] Rui Meng,[a] Baoda Xue,[b] Huiqiong Zhou,[b] Zhiyong Tang[b] and Yuan Zhang*[a]

Received 27th November 2018,
Accepted 11th January 2019

DOI: 10.1039/c8cp07271j

rsc.li/pccp

Here based on integral microcrystal (IMC) thin films of halide perovskites containing formamidinium (FA)/methylammonium (MA) mixed cations, afforded by a facile approach combining an anti-solvent and inverse temperature crystallization, we investigate the impact of the addition of $MAPbBr_3$ on the phase, thermal and environmental stabilities as well as the opto-electronic properties in FA-based IMC films. By single-crystal XRD, FA based IMCs have been found to possess a perfect cubic structure showing a slight lattice contraction compared to pristine $FAPbI_3$ crystals. In conjunction with optical and electrical analyses, the essential role of the introduced MA and Br ions in stabilizing the black phase in FA-based IMCs has been clarified, which explains the observed enhancement of photoluminescence and reduced trap densities. We also achieve stable pure $FAPbI_3$ crystals that do not exhibit a yellow-phase transition after one month in air. By utilizing $(FAPbI_3)_{1-x}(MAPbBr_3)_x$ IMCs as the photo-absorber, we realize highly photo-responsive photodiodes with a satisfactory stability in air and thermal stability upon heating. Of interest, the best photoresponsivity exceeding 300 A W^{-1} is achieved upon appropriate air-exposure, which is among the highest values reported for FA-based perovskite photodetectors. The air-modified optoelectronic behaviour can be related to the trap passivation through the surface physisorption of the environmental O_2, leading to reduced trap densities and resultant harmful SRH recombination.

Introduction

Inorganic–organic hybrid lead halide perovskites have garnered tremendous research attention in recent years due to their merits in advanced opto-electronic applications with particularities of long carrier diffusion length, low exciton binding energy and bandgap tunability.[1–7] In practice, the characteristics of devices based on polycrystalline perovskite films are still limited by their morphological disorder and non-negligible level of traps.[8–11] These disadvantages can be bypassed in single crystals of perovskites possessing appreciably lowered trap densities with long-range structural ordering.[12–14] Among the array of halide perovskites in which the sizes of the organic anions are subject to the Goldschmidt tolerance factor, formamidinium (FA) lead iodides are one of the most attractive candidates for photovoltaic devices with a suitable band gap.[15–20] However, due to the large ionic size of FA that tends to cause lattice stress, a non-perovskite yellow (δ) phase near room temperature (RT) can be formed, which is perceived to be harmful for ultimate device characteristics in perovskite solar cells.[21–24] To tackle the issue of phase instability, doping with halide (bromide) and organic (*e.g.* methylammonium or MA) anions is often applied for the release of lattice stress, such that the FA containing perovskites can stabilize as the dominant α phase near RT.[25–29] Based on solution growth methods, *e.g.* inverse temperature crystallization, millimeter-size bulk crystals of FA based perovskites have been realized with an excellent phase stability, large carrier diffusion distance and lower density of traps.[25,30] However, these commonly-adopted crystallization procedures for bulk perovskite crystals are often time-consuming and lack the controllability of the sample thickness relevant to applications based on a sandwiched architecture. Besides, abundant surface traps can be present in these freestanding crystals, due to under-coordinated metal or organic cations which tend to induce the unfavorable effect of non-stoichiometry.[8,31] To date, representative photoresponsivities in devices based on polycrystalline perovskite films or bulk crystals range between

[a] *HEEGER Beijing Research & Development Center, School of Chemistry, Beihang University, Beijing 100191, China. E-mail: yuanzhang@buaa.edu.cn*
[b] *CAS Key Laboratory of Nanosystem and Hierarchical Fabrication, CAS Center for Excellence in Nanoscience, National Center for Nanoscience and Technology, Beijing 100190, China*

† Electronic supplementary information (ESI) available. See DOI: 10.1039/c8cp07271j

0.1–100 A W^{-1} in the presence of high densities of traps.[32–34] Hu *et al.*[33] fabricated the first organic–inorganic hybrid perovskite photodetector with a responsivity of 3.49 A W^{-1} at 780 nm. As reported by Yan *et al.*,[34] a high-performance planar photodetector showing a responsivity of 7.92 A W^{-1} was fabricated on the (100) facet of a bulk $CH_3NH_3PbI_3$ perovskite single crystal. The relatively poor responsivity and time-consuming material growth may impose challenges on realistic opto-electronic applications based on bulk crystals. In this context, obtaining a fast crystallization for large area FA-IMCs with the controllability of trap levels is highly desirable. The rapid crystal growth method based on an anti-solvent vapor-assisted crystallization has been demonstrated to obtain large-size perovskite single crystals with MA ions.[35] Moreover, all-inorganic IMCs containing C anions have been demonstrated through a facile inverse temperature crystallization, leading to a high photoresponsivity for photodectors.[11] While impressive figures of merit have been demonstrated in these IMCs with large bandgaps, there are practical needs for opto-electronic responses of IMCs in the near infrared (IR) spectral regime. For this purpose, FA based IMCs with mixed ions will be ideal candidates for excellent photo-detectors due to the suitable bandgap.

Here we report a fast crystal growth methodology combining an anti-solvent and inverse temperature crystallization to obtain large-area FA-based perovskite integral microcrystals (IMCs) with low trap densities that exhibit excellent air- and thermal stabilities. By utilizing $(FAPbI_3)_{1-x}(MAPbBr_3)_x$ IMCs as the photo-absorber, we succeed in realizing highly photo-responsive photo-diodes with minimal degradation in air or upon heating. We achieve the best photoresponsivity exceeding 300 A W^{-1} upon appropriate air-exposure, which is among the highest values reported for FA-based perovskite photodetectors. The air-modified optoelectronic behavior can be related to the trap passivation through surface physisorption of the environmental O_2, leading to reduced trap densities and resultant harmful SRH recombination.

Results and discussion

The adopted procedure to obtain FA-IMCs is schematically illustrated in Fig. 1. To start, 0.2 M formamidinium lead iodide ($FAPbI_3$) mixed with different molar ratios (x) of methylammonium bromide ($MAPbBr_3$) (x = 0, 0.05, 0.1, 0.15) were dissolved in γ-butyrolactone (GBL, AR, ≥99%) to form a precursor solution and then toluene was added as an anti-solvent to reach the saturation point. Initially, a large amount of quantum dot nanocrystal nucleation was created in the saturated state. After heating up the solution at 120 °C with stirring, the nucleation site became abruptly enlarged, leading to micro-nanocrystals under inverse temperature conditions. In about 3 min, larger sized crystals were deposited on the substrates pre-patterned with ITO electrodes. After the solution became clear again, the substrates deposited with the crystals were carefully removed from the precursor solution and thermally annealed at

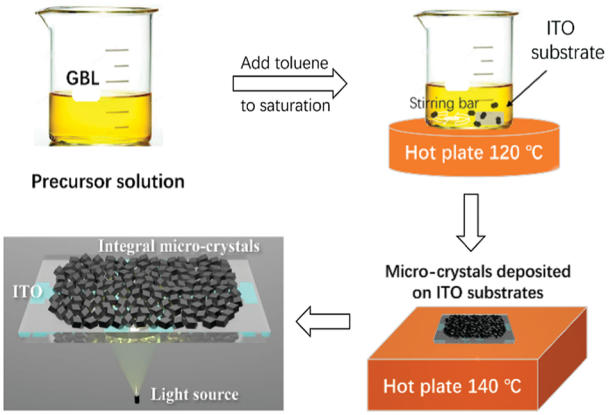

Fig. 1 Schematic illustration of the FA-based perovskite micro-crystal preparation and device measurement.

140 °C (15 min) to remove the solution residues (see more details in Fig. S1 in ESI†). Finally, high quality monocrystalline IMCs containing FA cations were obtained atop the ITO substrates forming an intimate contact (see Fig. 1).

To allow for a direct assessment of the film morphology of the obtained crystals, Fig. 2a–d show top-view images of $FAPbI_3$ and $(FAPbI_3)_{0.85}(MAPbBr_3)_{0.15}$ IMC films using field-emission scanning electron microscopy (FESEM). In both pristine and $MAPbBr_3$-doped (x = 0.15) $FAPbI_3$ IMCs, we observe dodecahedral structures. The main distinctions lie in the dimensions of the miniature perovskite single crystals which visibly reduce in the IMCs with mixed FA/MA cations. For example, the average crystal size is 30 μm in pristine $FAPbI_3$ and shrinks to 10 μm in $(FAPbI_3)_{0.85}(MAPbBr_3)_{0.15}$. Despite the smaller crystal size, the continuity between the interconnecting crystallites favorably increases with the mixed cations, exhibiting more compact features with fewer pinholes. These observations can imply high quality perovskite IMCs obtained by the combined anti-solvent and inverse temperature crystallization method. Fig. 2b and d display the zoomed-in SEM images. As can be seen, a reduced homogeneity in the size distribution in $(FAPbI_3)_{0.85}(MAPbBr_3)_{0.15}$ is noted. This trend may be understood by the enlarged non-uniformity in nucleation with the present mixed halogen ions. It should be mentioned that the reduced uniformity in size distribution may not be a hindrance for the carrier transport and adversely it may allow for an improved interconnection between individual crystallites. This is because those crystallites with smaller sizes may fill the spatial gaps between large-sized crystallites. As will be seen, such morphological features help reduce the structural defects.

Next, we performed a microscopic elemental analysis using energy dispersive spectrometry (EDS) to examine if $MAPbBr_3$ was truly incorporated into the crystals as a component instead of being washed off during the rinsing steps. By taking one single crystal of $FAPbI_3$ (Fig. 2e) and $(FAPbI_3)_{0.85}(MAPbBr_3)_{0.15}$ (Fig. 2f) as examples, the differentiated elemental weight percentages and elemental mapping of lead [Pb], iodine [I] and bromine [Br] can provide solid evidence for the presence of $MAPbBr_3$. As seen from Fig. 2e and f, we observe an obvious

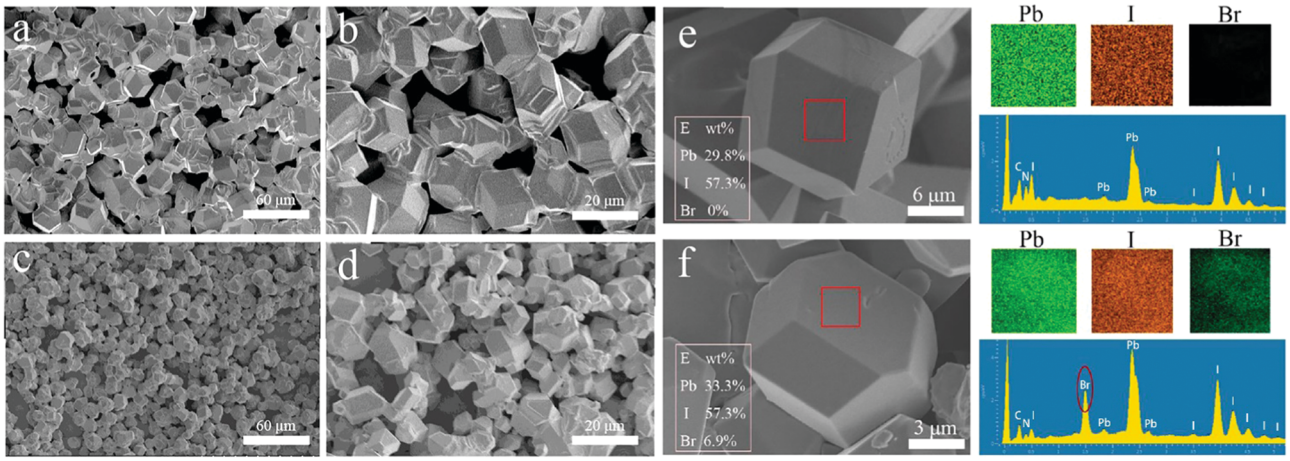

Fig. 2 (a–d) Top-view SEM images of IMCs based on $FAPbI_3$ (a and b) and $(FAPbI_3)_{0.85}(MAPbBr_3)_{0.15}$ (c and d) of different scan sizes. (e and f) The EDS element analysis of one single crystal of $FAPbI_3$ (e) and $(FAPbI_3)_{0.85}(MAPbBr_3)_{0.15}$ IMCs. Also shown by the graphs on the right are the elemental weight percentages and elemental mapping distributions of Lead [Pb], Iodine [I] and Bromine [Br].

bromine [Br] peak together with a uniform [Br] elemental distribution in the sample of $(FAPbI_3)_{0.85}(MAPbBr_3)_{0.15}$. This infers the presence of $MAPbBr_3$ in the octahedral cage.[36–38] We further calculated the ratio of the [I]/[Br] peak percentage which is 57.3%/6.9% (see inset of Fig. 2f, molar ratio of [I] : [Br] = 5 : 1). This result agrees with the corresponding theoretical value of the $PbBrI_5$ octahedral cage in which one iodine element should be replaced by one bromine element in every PbI_6 cage after doping. From the EDS analysis, we derive an important indication that the effect of non-stoichiometry on the IMCs based on $(FAPbI_3)_{0.85}(MAPbBr_3)_{0.15}$ is minimized.

We further examined the structural properties in our samples from the performed powder X-ray diffraction (XRD) patterns as shown in Fig. 3a. The results indicate that $MAPbBr_3$ has been added to $FAPbI_3$ to form hybrid ion crystals. Generally, δ-phase $FAPbI_3$ perovskites tend to be generated even before thermal annealing (see optical image in Fig. S1, ESI†) and the resultant decomposition should be visibly reflected by the characteristic

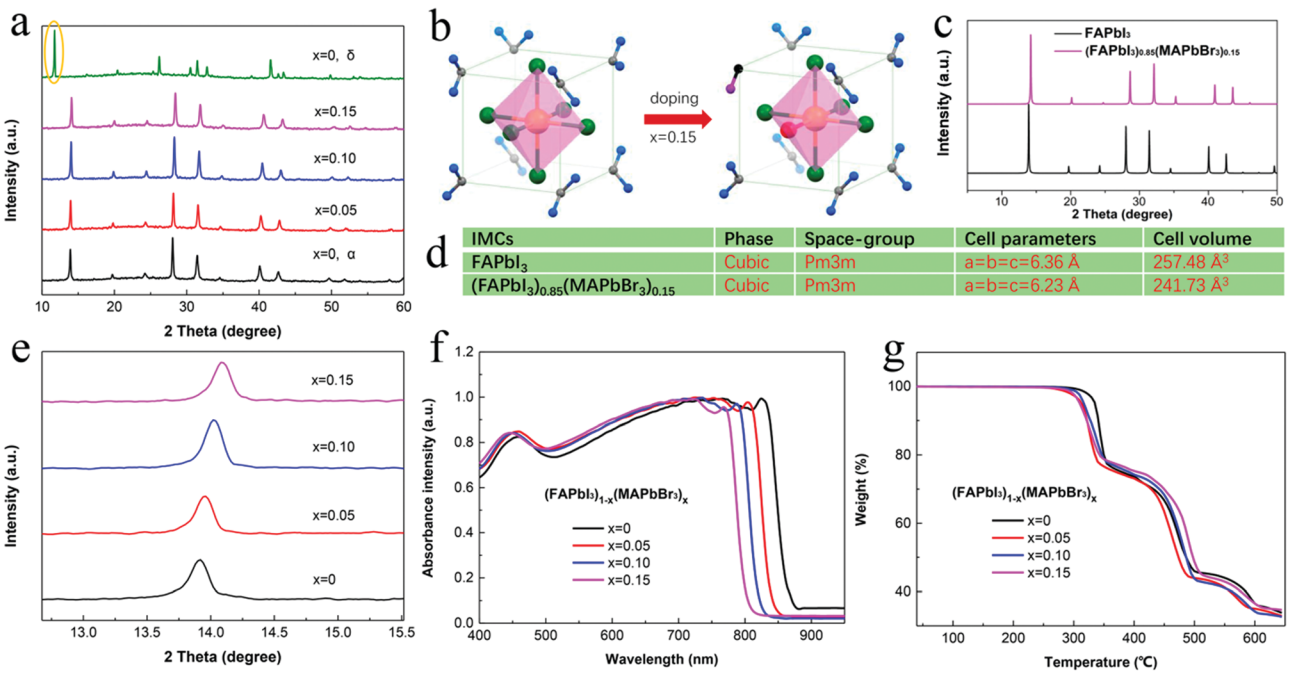

Fig. 3 (a) Powder X-ray diffraction (XRD) patterns of $(FAPbI_3)_{1-x}(MAPbBr_3)_x$ IMCs with different doping levels (x = 0–0.15) and δ-$FAPbI_3$. (b) Crystal structure transformation from $FAPbI_3$ to $(FAPbI_3)_{0.85}(MAPbBr_3)_{0.15}$ (yellow, lead; green, iodine; grey and blue, FA; red, bromine; black and pink, MA). (c) Powder XRD predicted by calculation. (d) Cell parameters of $FAPbI_3$ and $(FAPbI_3)_{0.85}(MAPbBr_3)_{0.15}$. (e) X-ray diffraction patterns of the (100) reflection as a function of composition for $(FAPbI_3)_{1-x}(MAPbBr_3)_x$ IMCs (x = 0–0.15). (f) The UV–IR absorption spectra with the Tauc Plot embedded in. (g) Thermogravimetric analysis of $(FAPbI_3)_{1-x}(MAPbBr_3)_x$ IMCs (x = 0–0.15).

XRD peaks around 12 degrees, originating from PbI_2. However, in our case we cannot observe the XRD peaks ascribed to δ-phase after 140 °C of annealing, regardless of the addition of $MAPbBr_3$. This suggests the formation of high-quality black phase $(FAPbI_3)_{1-x}(MAPbBr_3)_x$ IMCs afforded by the described fast crystallization approach.

Next, we performed single crystal XRD to explore the lattice structure of the IMCs impacted by the incorporated $MAPbBr_3$ (see Fig. 3b–d). Detailed cell parameters extracted from the single crystal XRD analysis are provided in the inset of Fig. 3d. We resolved a perfect cubic structure (*Pm3m* space-group) in both $FAPbI_3$ and $(FAPbI_3)_{0.85}(MAPbBr_3)_{0.15}$ crystals. With respect to the predicted powder XRD patterns as shown in Fig. 3c, we found a perfect match between the calculated and experimentally obtained XRD patterns, confirming the cubic lattice structure. In concert to previous studies based on FA single crystals,[38] the $(FAPbI_3)_{0.85}(MAPbBr_3)_{0.15}$ single crystals are associated with a smaller cell volume (241.73 $Å^3$) with $a = b = c = 6.23$ Å, compared to $FAPbI_3$ (257.48 $Å^3$) with $a = b = c = 6.36$ Å. The trend in the cell contraction is in line with the enlarged powder XRD patterns as shown in Fig. 3e. For example, with the increase of $MAPbBr_3$ the peak at 13.9 degree (in the absence of $MAPbBr_3$) progressively shifts toward higher angles. This behavior can be correlated to the decrease of lattice constant in $(FAPbI_3)_{0.85}(MAPbBr_3)_{0.15}$. As it has been argued, with partially substituted FA ions by MA^+, the cubic structure in FA-based single crystals can be stabilized due to the adjusted Goldschmidt tolerance factor,[39] governed by the reduced radii of MA (213 pm) with respect to FA (253 pm). The gain in stability also can be ascribed to the increased entropy in the perovskite containing FA–MA mixed ions with higher degrees of MA^+ disorder.[39] Our single crystal XRD data point at the necessity of incorporating the MA and Br cations to achieve favourable structural meliorations for an improved phase stability in FA-based IMCs.

Another benefit of adding $MAPbBr_3$ to $FAPbI_3$ crystals has been found in the changed bandgap.[40,41] In this regard, we measured the UV–IR absorption of FA-based IMCs with different $MAPbBr_3$ concentrations. As shown in Fig. 3f, we observe a progressive blueshift in the absorption cut-off between 790–850 nm with an incrementally varied $MAPbBr_3$ ratio. The bandgap (E_g) in $(FAPbI_3)_{1-x}(MAPbBr_3)_x$ crystals was estimated from the well-established Tauc plot as shown in Fig. 3f inset. The determined E_g is 1.44 eV, 1.48 eV, 1.52 eV, and 1.54 eV for $x = 0$, 0.05, 0.10, and 0.15, respectively. The systematic tuning on the absorbance *via* bandgap engineering enables different spectral responses to be obtained in devices based on FA-containing IMCs.

One of the key merits of single crystal perovskites over their polycrystalline alternatives is the enhanced environmental stability, due to increased structural ordering with reduced defects. To demonstrate this advantage, we exposed our IMCs to air for a month (humidity = 15%) and measured the XRD patterns afterward. Surprisingly, all the studied IMCs did not show any severe degradation upon air-exposure after one month. As shown by the XRD patterns in Fig. S2 in ESI,† the peak assigned to PbI_2 did not show up in the aged crystals, evidencing the absence of phase transition. As an affirmation, we comparatively measured the UV–IR absorption spectra of freshly grown and air-stored IMCs. Again, no visible shifts in the absorption edge can be noted (see Fig. S3, ESI†). These results imply the high moisture tolerance in our FA-based IMCs with a satisfactory air-stability. In previous studies, it has been shown that the doping of $MAPbBr_3$ could contribute to the black phase stability in $FAPbI_3$ perovskite films at room temperature (RT).[3] However, in our IMCs comprising $(FAPbI_3)_{1-x}(MAPbBr_3)_x$ with different concentrations of $MAPbBr_3$, we do not observe any noticeable phase transition with the appearance of the yellow phase at RT (Fig. S2, ESI†), indicating an excellent black phase stability under ambient conditions. Regardless of the origins, the superior phase stability of $FAPbI_3$ crystals afforded by the described crystal growth method has not been reported before. Generally, single crystals prepared by the conventional solution processes tend to experience a yellow phase transition in a short period, *e.g.* one day.[3,38] For defect-rich polycrystalline films, the detrimental yellow phase can be observed even within minutes. It is commonly accepted that the phase transition rate in $FAPbI_3$ could depend on the crystal quality, *e.g.* the trap level.[3,38] To this end, the retardation of the phase transition with the dominant black phase may point to the high crystal quality in our FA-based IMCs, which will be further evidenced.

The thermal stability of $(FAPbI3)_{1-x}(MAPbBr_3)_x$ IMCs at different doping concentrations was examined by thermogravimetric (TG) analysis (see results in Fig. 3g). With the introduced $MAPbBr_3$, we observe more pronounced degradations at a higher temperature (see more details in Fig. S4, ESI†). The poorer thermal stability in the crystal with mixed FA/MA cations may be interpreted in terms of the stronger tendency of thermal decomposition in $MAPbBr_3$, compared to pristine $FAPbI_3$. In practice, optimizing the balance between thermal and phase stabilities in IMCs needs fine control over the compositional ratio between $FAPbI_3$ and $MAPbBr_3$.

The remarkable performance of hybrid perovskite photovoltaics to a large degree can be attributed to their long PL lifetime and resultant superior diffusion distance. In this context, we measured the steady-state photoluminescence spectra (under 532 nm excitation) of FA-based IMCs with different concentrations of $MAPbBr_3$ and the results are displayed in Fig. 4a. Of interest, the PL intensity becomes considerably enhanced at increased doping levels *e.g.* the strongest PL was found at $x = 0.15$, showing a monotonic change. This phenomenon highlights the capability of the incorporated MA^+ and Br^+ cations in suppressing nonradiative recombination channels in the FA-based crystal, possibly related to the mitigation of trapping. The result of PL is in line with the identified structural modifications with $MAPbBr_3$, showing fewer pinholes and more dense features. Fig. 4b shows time-resolved PL spectroscopy of $(FAPbI_3)_{1-x}(MAPbBr_3)_x$ crystals ($x = 0.05$–0.15). We cannot accurately determine the PL lifetime in pristine $FAPbI_3$ using our spectrometer, due to the ultrafast decay time and weak PL intensity, while the trend of longer-lived PL decay at higher ratios of $MAPbBr_3$ is clearly observed. For example, the PL lifetimes of $(FAPbI_3)_{1-x}(MAPbBr_3)_x$ IMCs ($x = 0.15$) were

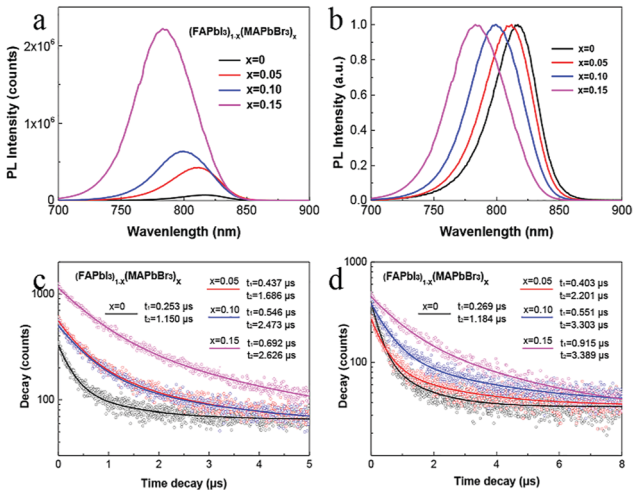

Fig. 4 (a) Steady-state photoluminescence (PL) spectra of $(FAPbI_3)_{1-x}$-$(MAPbBr_3)_x$ IMCs on a silica substrate. (a) Non-normalized and (b) normalized. Time-resolved PL spectroscopy of (c) freshly grown and (d) aged (with 7 days of air-exposure) single crystals of $(FAPbI_3)_{1-x}(MAPbBr_3)_x$ at different doping concentrations.

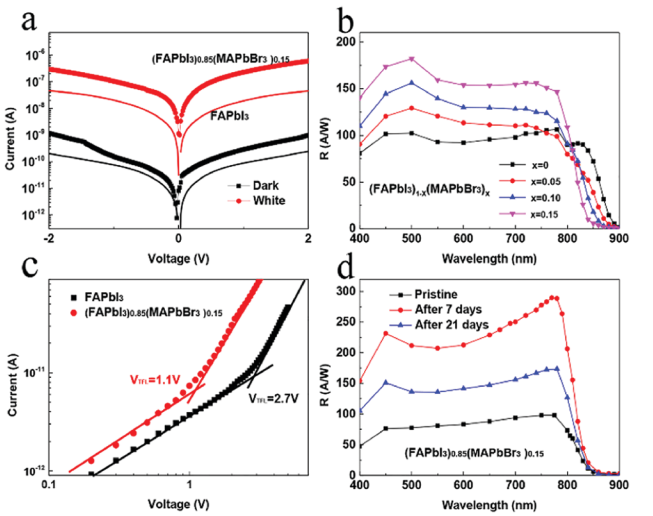

Fig. 5 (a) Current *versus* voltage characteristics of $(FAPbI_3)_{0.85}(MAPbBr_3)_{0.15}$ based IMC photodetectors in the dark and under white light irradiation. (b) The spectral response of IMC devices under monochromatic light based on freshly grown $(FAPbI_3)_{1-x}(MAPbBr_3)_x$ (x = 0–0.15) (devices electrodes W/L = 5 μm/1000 μm). (c) Dark current of planar diodes based on freshly grown $FAPbI_3$ and $(FAPbI_3)_{0.85}(MAPbBr_3)_{0.15}$ IMCs. (Device electrodes W/L = 100 μm/1000 μm). (d) Comparison of the spectral response of IMC devices under monochromatic light based on $(FAPbI_3)_{0.85}(MAPbBr_3)_{0.15}$ without and after air-exposure. Devices adopted interdigitated electrodes with W = 10 μm and L = 8000 μm.

determined to be 0.692 μs and 2.626 μs in the fast and slow decay regimes, arising from the recombination at the surface and bulk region, respectively.[10,35] The longer-lived PL at both temporal regimes provides the signature of reduced trap densities in the bulk or surface area in our IMCs with mixed cations.

We also examined the crystals after being exposed to air for 7 days (see Fig. 4d). A resembling tendency of increased PL lifetime is observed in all the $(FAPbI_3)_{1-x}(MAPbBr_3)_x$ crystals. This is similar to $MAPbBr_3$, where longer-lived PLs can be noted.

In a previous study based on $MAPbI_3$ crystals, a similar phenomenon with an enlarged PL intensity in association with longer-PL lifetimes was observed, attributed to the passivation of traps *via* physically adsorbed O_2 on the perovskite surface.[42] As will be seen, this useful modification by air interestingly has led to an enhanced opto-electronic response in our IMCs. Also, incorporating the IMC as the photoactive layer is of advantage in suppressing the dark current[11] because the ITO-perovskite interface is expected to produce a rectifying junction due to an unmatched work function, enabling fabrication of metal–semiconductor–metal photodetectors.[10] On this basis, we utilized $(FAPbI_3)_{1-x}(MAPbBr_3)_x$ (x = 0 and 0.15) as the photoactive layers and evaluated the photoresponse in planar diodes. Fig. 5a shows current *versus* voltage (*I–V*) characteristics of diodes with parallel-shaped ITO contacts. A considerable photoresponse to white light irradiation is observed in both devices with x = 0 and 0.15, exhibiting large I_{light}/I_{dark} ratios of more than two orders. The slight increase in the dark current in the presence of $MAPbBr_3$ agrees with the SEM images in which an improved continuity was observed. The low dark current ($\sim 10^{-10}$ A) can be related to the crystal-to-crystal interfaces/gaps present in our IMCs, effectively impeding the transport by background carriers.[35] Remarkably, the device with x = 0.15 displays an enlarged photocurrent, which can be primarily ascribed to the reduced charge trapping, as revealed by the enhanced PL lifetime. As a result, a longer travel distance for photo-generated carriers may be realized, which is beneficial for the charge sweepout and eventual photocurrent. Fig. 5b displays the spectral response of planar diodes based on various $(FAPbI_3)_{1-x}(MAPbBr_3)_x$ IMCs (x = 0–0.15) under monochromatic irradiation conditions. The spectral shape approximately follows its respective absorption profiles, showing blue-shifts in the light response edge with an increased $MAPbBr_3$ concentration. The flattened response in the above-gap absorption regime allows for a broadband detection mode with these IMCs. It is interesting to note that the photoresponsivity R (defined as $R = I_{light} - I_{dark}/P_{light}$, where P_{light} is the light intensity) can be tuned *via* the concentration of $MAPbBr_3$. In the best case, the R can exceed 150 A W^{-1} at around 500 nm with x = 0.15.

The passivation of perovskites to mitigate the impact of traps is critical for obtaining satisfactory device performance.[43–45] To understand the mechanism of the enlarged photoresponse in the presence of $MAPbBr_3$, we compared the dark currents by using $FAPbI_3$ and $(FAPbI_3)_{0.85}(MAPbBr_3)_{0.15}$ as the active layers (see results in Fig. 5c). Obviously, the current increases with the addition of $MAPbBr_3$, likely attributed to an enhanced electrical conductivity. In both devices, the transition from the ohmic current (originating from those background carriers in the crystal) to the trap-filling current (TFC) is clearly witnessed with increasing bias. From the voltage corresponding to this transition (V_{tr}), the trap density can be roughly estimated, according to the relation,[10]

$$N_{trap} = \frac{2\varepsilon V_{tr}}{qL^2} \quad (1)$$

where ε is the dielectric constant of perovskites ($\sim$25), q is the elemental charge and L is the length of the solid under test. The V_{tr} becomes smaller from 2.7 V (pristine crystal) to 1.1 V (with doping). Based on the result of V_{tr}, the trap density was determined to be 7.5×10^{11} cm^{-3} (pristine) and 3.0×10^{11} cm^{-3} (with 15% doping) from eqn (1). The reduction of trap density favorably decreases the Shockley–Read–Hall recombination, such that larger amounts of photo-generated carriers can be extracted toward the electrodes. This rationale explains the enhanced photocurrent and resultant R. Of interest, we found that the trap concentration is inversely proportional to the ratio of $MAPbBr_3$. This provides an interesting route to mediate nonradiative recombination and resulting carrier losses in IMC based photonic devices.

In light of the enhanced PL properties with longer PL decays in the crystals stored in air, finally we examined the impact of air-exposure on the photoresponse in our planar diodes. Fig. 5d displays the determined R of IMC diodes comprising freshly grown and air-exposed $(FAPbI_3)_{0.85}(MAPbBr_3)_{0.15}$ crystals. Of interest, the R receives a considerable boost, from 100 A W^{-1} to 300 A W^{-1} when storing the crystals in air for about 1 week and then adversely decreases upon further exposure to ambient conditions. The achieved R of 300 A W^{-1} is among the highest values reported on FA-based perovskite photodetectors so far.[46,47] The air-modified photoresponse has been reproducibly seen in IMCs with different concentrations of $MAPbBr_3$ (see Fig. S7, ESI†). Indicated by the dark transport measurements as shown in Fig. S8, ESI,† this phenomenon can be related to the further suppression of charge trapping, as revealed by the decrease of V_{tr} with appropriate exposure to air. This favorable modification can be explained by the effect of O_2-adsorption on the surface of perovskite IMCs or regions neighboring to the bottom ITO contacts. To confirm the influence of O_2, we carefully transferred the aged device (after air-storage for 35 days) to a vacuum probe station for a few hours. As shown in Fig. S9, ESI,† the device with re-evacuation can roughly recover to its initial status, yielding a similar photoresponse to the fresh device. On the other hand, the photoluminescence of IMCs with different MA concentrations hardly changes (see Fig. S10, ESI†), confirming the insignificant air-degradation in our sample. This reproducible behavior of R can be explained by the desorption of O_2 molecules at the surface or also at the bulk region of FA-based crystals. At this moment, how water molecules influence R is not fully understood. But in our recent study on $MAPbI_3$ single crystals, we found that H_2O can cause severe degradation of the crystal quality with a reduced PL lifetime.[48] On this basis, the reduced R with excess air-exposure might be linked to the negative effects of moisture on our samples. Further improvements in the environmental stability of FA-based IMCs could be promoted by the application of a hydrophobic protection layer with Lewis acid functional groups to render desired surface trap passivation.

Conclusions

In summary, we report high quality and phase-stable FA-based perovskite integral-micro-crystals (IMCs) afforded by using a facile method combining an anti-solvent and inverse temperature crystallization. Single crystal XRD and EDS measurements evidence the incorporation of $MAPbBr_3$ into the matrix of $FAPbI_3$ crystals, showing a perfect cubic cell structure with a slightly reduced cell volume. This result in conjunction with comprehensive optical and electrical analyses unveils the role of MA and Br in stabilizing the black phase in FA-based IMCs, leading to an increased PL lifetime, and a reduced trap density with a gain in phase-stability. We have succeeded in realizing a series of highly photo-responsive IMCs based on $(FAPbI_3)_{1-x}(MAPbBr_3)_x$ photo-absorbers, showing satisfactory environmental stability in air and thermal stability upon heating. The realized best photo-responsivity in a planar device configuration exceeds 300 A W^{-1}, which is among the highest values reported on FA-based perovskite photodetectors so far. Upon appropriate air-exposure, we found that the trap level and the resultant photo-responsive behaviour of IMC-based planar diodes can be modulated, which is a result of the effective trap passivation with O_2-adsorption. The obtained improvements in the photoresponsivity and stability enrich our understanding of the key opto-electrical properties in $(FAPbI_3)_{1-x}(MAPbBr_3)_x$ perovskites, which are the state-of-the art material candidates for high performance perovskite solar cells and relevant photonic devices.

Experimental

Materials

Commercialized materials. $PbBr_2$, PbI_2 ($\geq$98%, Alfa Aesar), FAI (Greatcellsolar), MAI (Dyesol), toluene and γ-GBL (AR, $\geq$99%, Aladdin Co., Ltd, China) were used as received without further purification.

Device fabrication

Glass substrates with redeposited ITO electrodes were patterned using the dry etching method. A layer of $(FAPbI3)_{1-x}(MAPbBr_3)_x$ IMCs was then deposited on the substrate using the method described above.

Device testing and material characterization

$(FAPbI_3)_{1-x}(MAPbBr_3)_x$ IMC SEM images were captured using a Hitachi S4800 electron microscope. EDS was measured on a Hitachi-SU8220 microscope. Powder XRD was measured by using a Rigaku (model: D/MAX-TTRIII) X-ray diffractometer equipped with a gobble mirror and a monochromatic CuKα (λ = 1.5405 Å) radiation source. The UV–IR spectroscopy was obtained using a UV–vis spectrometer (the PerkinElmer Lambda 650/850/950 UV–vis spectrophotometer) in the 400–950 nm wavelength range. The steady-state PL excitation and emission spectra were recorded by a HORIBA Fluorolog-III spectrofluorometer housed with a Janis cryostat by 532 nm excitation light. The PL decay kinetics were measured using a HORIBA Jobin-Yvon Fluorolog-III fluorimeter in transient mode with the excitation provided by a 509 nm semiconductor diode laser. The PL decay was acquired with a peak pre-set of 3000 counts and the data were analysed using the Data Analysis Software. Single crystal XRD was

performed on a Rigaku AFC-10/Saturn 724 + CCD diffractometer with graphite-monochromatic Mo Kα radiation (λ = 0.71073 Å) using the multi-scan technique. The structures were determined by direct methods using SHELXS-971 and refined by full-matrix least-squares procedures on F^2 with SHELXL-97. All non-hydrogen atoms were obtained from the differences in Fourier map and subjected to anisotropic refinement by full-matrix least squares on F^2. Hydrogen atoms were obtained geometrically and treated as riding on the parent atoms or were constrained in the locations during refinements.

I–V characteristics of planar diodes were measured in a LakeShore vacuum probe station without evacuation (for testing the device air-stability) or under vacuum (for the desorption of O_2) using a Keithley 4200-SCS semiconductor analyser under irradiation sourced by a Zolix monochromator (Omni-λ 300). The light intensity was calibrated by a Thorlabs power meter.

Conflicts of interest

There are no conflicts to declare.

Acknowledgements

This work was supported by the National Natural Science Foundation of China (NSFC) (No. 21875012 and 21674006). Y. Z acknowledges the 111 Project (B14009). H. Zhou thanks the National Key Research and Development Program of China (2017YFA0206600).

References

1 M. Liu, M. B. Johnston and H. J. Snaith, *Nature*, 2013, **501**, 395.
2 N. J. Jeon, J. H. Noh, Y. C. Kim, W. S. Yang, S. Ryu and S. I. Seok, *Nat. Mater.*, 2014, **13**, 897.
3 N. J. Jeon, J. H. Noh, W. S. Yang, Y. C. Kim, S. Ryu, J. Seo and S. I. Seok, *Nature*, 2015, **517**, 476.
4 G. E. Eperon, V. M. Burlakov, P. Docampo, A. Goriely and H. J. Snaith, *Adv. Funct. Mater.*, 2014, **24**, 151–157.
5 Y. C. Kim, T. Y. Yang, N. J. Jeon, J. Im, S. Jang, T. J. Shin, H. W. Shin, S. Kim, E. Lee, S. Kim, J. H. Noh, S. I. Seok and J. Seo, *Energy Environ. Sci.*, 2017, **10**, 2109–2116.
6 H. Zheng, G. Liu, L. Zhu, J. Ye, X. Zhang, A. Alsaedi, T. Hayat, X. Pan and S. Dai, *Adv. Energy Mater.*, 2018, 1800051.
7 S. You, H. Wang, S. Bi, J. Zhou, L. Qin, X. Qiu, Z. Zhao, Y. Xu, Y. Zhang, X. Shi, H. Zhou and Z. Tang, *Adv. Mater.*, 2018, **30**, 1706924.
8 C. Bi, Q. Wang, Y. Shao, Y. Yuan, Z. Xiao and J. Huang, *Nat. Commun.*, 2015, **6**, 7747.
9 Y. Shao, Y. Fang, T. Li, Q. Wang, Q. Dong, Y. Deng, Y. Yuan, H. Wei, M. Wang, A. Gruverman, J. Shield and J. Huang, *Energy Environ. Sci.*, 2016, **9**, 1752–1759.
10 M. I. Saidaminov, V. Adinolfi, R. Comin, A. L. Abdelhady, W. Peng, I. Dursun, M. Yuan, S. Hoogland, E. H. Sargent and O. M. Bakr, *Nat. Commun.*, 2015, **6**, 8724.
11 B. Yang, F. Zhang, J. Chen, S. Yang, X. Xia, T. Pullerits, W. Deng and K. Han, *Adv. Mater.*, 2017, **29**, 1703758.
12 Y. Yang, Y. Yan, M. Yang, S. Choi, K. Zhu, J. M. Luther and M. C. Beard, *Nat. Commun.*, 2015, **6**, 7961.
13 J.-S. Park, S. Choi, Y. Yan, Y. Yang, J. M. Luther, S.-H. Wei, P. Parilla and K. Zhu, *J. Phys. Chem. Lett.*, 2015, **6**, 4304–4308.
14 B. Wu, H. T. Nguyen, Z. Ku, G. Han, D. Giovanni, N. Mathews, H. J. Fan and T. C. Sum, *Adv. Energy Mater.*, 2016, **6**, 1600551.
15 M. Saliba, T. Matsui, J. Y. Seo, K. Domanski, J. P. Correa-Baena, M. K. Nazeeruddin, S. M. Zakeeruddin, W. Tress, A. Abate, A. Hagfeldt and M. Gratzel, *Energy Environ. Sci.*, 2016, **9**, 1989–1997.
16 Y. Wu, X. Yang, W. Chen, Y. Yue, M. Cai, F. Xie, E. Bi, A. Islam and L. Han, *Nat. Energy*, 2016, **1**, 16148.
17 L. Meng, E. P. Yao, Z. Hong, H. Chen, P. Sun, Z. Yang, G. Li and Y. Yang, *Adv. Mater.*, 2017, **29**, 1603826.
18 M. I. Saidaminov, A. L. Abdelhady, B. Murali, E. Alarousu, V. M. Burlakov, W. Peng, I. Dursun, L. Wang, Y. He, G. Maculan, A. Goriely, T. Wu, O. F. Mohammed and O. M. Bakr, *Nat. Commun.*, 2015, **6**, 7586.
19 C. Mu, J. Pan, S. Feng, Q. Li and D. Xu, *Adv. Energy Mater.*, 2017, **7**, 1601297.
20 H. Zheng, G. Liu, C. Zhang, L. Zhu, A. Alsaedi, T. Hayat, X. Pan and S. Dai, *Sol. Energy*, 2018, **159**, 914–919.
21 F. Ji, L. Wang, S. Pang, P. Gao, H. Xu, G. Xie, J. Zhang and G. Cui, *J. Mater. Chem. A*, 2016, **4**, 14437–14443.
22 Z. Wang, D. P. McMeekin, N. Sakai, S. van Reenen, K. Wojciechowski, J. B. Patel, M. B. Johnston and H. J. Snaith, *Adv. Mater.*, 2017, **29**, 1604186.
23 D. Prochowicz, P. Yadav, M. Saliba, M. Saski, S. M. Zakeeruddin, J. Lewiński and M. Grätzel, *Sustainable Energy Fuels*, 2017, **1**, 689–693.
24 N. Li, Z. Zhu, C.-C. Chueh, H. Liu, B. Peng, A. Petrone, X. Li, L. Wang and A. K. Y. Jen, *Adv. Energy Mater.*, 2017, **7**, 1601307.
25 J.-W. Lee, D.-H. Kim, H.-S. Kim, S.-W. Seo, S. M. Cho and N.-G. Park, *Adv. Energy Mater.*, 2015, **5**, 1501310.
26 G. E. Eperon, C. E. Beck and H. J. Snaith, *Mater. Horiz.*, 2016, **3**, 63–71.
27 M. Long, T. Zhang, W. Xu, X. Zeng, F. Xie, Q. Li, Z. Chen, F. Zhou, K. S. Wong, K. Yan and J. Xu, *Adv. Energy Mater.*, 2017, **7**, 1601882.
28 D. J. Kubicki, D. Prochowicz, A. Hofstetter, M. Saski, P. Yadav, D. Bi, N. Pellet, J. Lewiński, S. M. Zakeeruddin, M. Grätzel and L. Emsley, *J. Am. Chem. Soc.*, 2018, **140**, 3345–3351.
29 N. F. Montcada, M. Mendez, K. T. Cho, M. K. Nazeeruddin and E. Palomares, *Nanoscale*, 2018, **10**, 6155–6158.
30 J.-W. Lee, S.-G. Kim, S.-H. Bae, D.-K. Lee, O. Lin, Y. Yang and N.-G. Park, *Nano Lett.*, 2017, **17**, 4270–4276.
31 Y. Fang, Q. Dong, Y. Shao, Y. Yuan and J. Huang, *Nat. Photonics*, 2015, **9**, 679.
32 L. Dou, Y. Yang, J. You, Z. Hong, W.-H. Chang, G. Li, Y. Yang, W. Wang, Y. Ma and L. Qi, *Adv. Funct. Mater.*, 2017, **27**, 1603653.

33 X. Hu, X. D. Zhang, L. Liang, J. Bao, S. Li, W. L. Yang and Y. Xie, *Adv. Funct. Mater.*, 2014, **46**, 7373–7380.
34 H. Fang, Q. Li, J. Ding, N. Li, H. Tian, L. Zhang, T. Ren, J. Dai, L. Wang and Q. Yan, *J. Mater. Chem. C*, 2016, **4**, 630.
35 M. I. Saidaminov, M. A. Haque, M. Savoie, A. L. Abdelhady, N. Cho, I. Dursun, U. Buttner, E. Alarousu, T. Wu and O. M. Bakr, *Adv. Mater.*, 2016, **28**, 8144–8149.
36 K. T. Cho, S. Paek, G. Grancini, C. Roldán-Carmona, P. Gao, Y. Lee and M. K. Nazeeruddin, *Energy Environ. Sci.*, 2017, **10**, 621–627.
37 W.-G. Li, H.-S. Rao, B.-X. Chen, X.-D. Wang and D.-B. Kuang, *J. Mater. Chem. A*, 2017, **36**, 19431–19438.
38 L. Q. Xie, L. Chen, Z. A. Nan, H. X. Lin, T. Wang, D. P. Zhan, J. W. Yan, B. W. Mao and Z. Q. Tian, *J. Am. Chem. Soc.*, 2017, **139**, 3320–3323.
39 G. Kieslich, S. Sun and A. K. Cheetham, *Chem. Sci.*, 2014, **5**, 4712–4715.
40 W. S. Yang, J. H. Noh, N. J. Jeon, Y. C. Kim, S. Ryu, J. Seo and S. I. Seok, *Science*, 2015, **348**, 1234–1237.
41 M. I. Saidaminov, A. L. Abdelhady, G. Maculan and O. M. Bakr, *Chem. Commun.*, 2015, **51**, 17658–17661.
42 D. Meggiolaro, E. Mosconi and F. De Angelis, *ACS Energy Lett.*, 2017, **2**, 2794–2798.
43 L. Shen, Y. Fang, D. Wang, Y. Bai, Y. Deng, M. Wang, Y. Lu and J. Huang, *Adv. Mater.*, 2016, **28**, 10794–10800.
44 L. Shen, Y. Lin, C. Bao, Y. Bai, Y. Deng, M. Wang, T. Li, Y. Lu, A. Gruverman, W. Li and J. Huang, *Mater. Horiz.*, 2017, **4**, 242–248.
45 Y. Lin, L. Shen, J. Dai, Y. Deng, Y. Wu, Y. Bai, X. Zheng, J. Wang, Y. Fang, H. Wei, W. Ma, X. C. Zeng, X. Zhan and J. Huang, *Adv. Mater.*, 2017, **29**, 1604545.
46 S. Li, S. Tong, J. Yang, H. Xia, C. Zhang, C. Zhang, J. Shen, S. Xiao, J. He, Y. Gao, B. Yang and J.-Q. Meng, *Org. Electron.*, 2017, **47**, 102–107.
47 F. X. Liang, J. Z. Wang, Z. X. Zhang, Y. Y. Wang, Y. Gao and L. B. Luo, *Adv. Opt. Mater.*, 2017, **5**, 1700654.
48 J. Zhou, H. H. Fang, H. Wang, R. Meng, H. Zhou, M. A. Loi and Y. Zhang, *ACS Appl. Mater. Interfaces*, 2018, **10**, 35580–35588.